Journal of Applied Automation Technologies

Research Paper

Gait-Adaptive Neural Operator for Snake Robots Using Proprioceptive Signals in Confined Spaces

Felicja Głębocka[1,*], Lech Cyprian Górski[1], Grzegorz Chmielewski[2] and Maria Kaczan[2]

[1] Faculty of Automatic Control, Robotics and Electrical Engineering, Poznan University of Technology, Poznan, 60-965, Poland
[2] Faculty of Electrical and Automatic Control Engineering, Czestochowa University of Technology, Czestochowa, 42-200, Poland
*Corresponding author: felicja.gleb@put.poznan.pl

Abstract. Confined industrial passages remain difficult for snake robots because contact forces, wall clearance, and body curvature change faster than vision-based planners can reliably update. This paper presents a gait-adaptive neural operator that converts proprioceptive streams into spatially continuous corrections for serpenoid amplitude, phase, and segmental impedance. Joint angle, motor current, link acceleration, and contact pressure are represented as body-coordinate fields, and the operator learns a corrective gait field without external localization. A bounded residual formulation keeps the learned correction compatible with rhythmic locomotion, actuator limits, and embedded control timing. Experiments were conducted in straight-pipe, elbow-pipe, rubble-slot, and cable-tray scenes with six clearance ratios, five friction levels, payload offsets, and injected sensing disturbances. Compared with fixed serpenoid, impedance-adaptive, and recurrent-policy baselines, the proposed operator increased mean traversal success from 71.4%, 82.6%, and 86.1% to 94.8%, reduced slip events by 39.7%, and lowered normalized transport cost by 18.9%. At a clearance ratio of 1.10, success reached 91.7%, while the strongest baseline reached 81.7%. The embedded GPU inference latency was 7.6 ms, supporting closed-loop updates at 80 Hz with timing margin for safety supervision. These results indicate that proprioceptive operator learning can support robust locomotion when visual sensing is intermittent, contaminated, or geometrically occluded.

Keywords: *Proprioceptive Sensing, Snake Robot, Neural Operator, Impedance Adaptation, Confined-Space Locomotion*

Received on 13 February 2026, Accepted on 20 June 2026, Published on 29 June 2026

Introduction

Snake robots have long been studied as mobile systems whose morphology is suitable for inspection, search-and-rescue, and maintenance tasks in geometrically restrictive environments [1]. Their slender articulated bodies can distribute contact across many links, allowing walls, pipe surfaces, and irregular debris to become useful sources of propulsion rather than unavoidable failure modes [2]. In underground ducts, petrochemical pipe racks, ventilation tunnels, and post-disaster voids, turning space is scarce, visual range is limited, and repeated contact with surfaces of unknown friction is common during deployment [3]. These conditions make locomotion a problem of continuously reshaping body waves while preserving traction and avoiding self-locking, rather than selecting a single nominal gait [4]. Classical serpenoid curves and central pattern generators remain appealing because their parameters are interpretable, but they usually assume a stable relation among amplitude, phase lag, and forward speed [5]. When the body is compressed in a narrow passage, this relation may break down because small segment motions can generate large contact impulses and asymmetric slip [6]. A controller for this setting therefore requires local mechanical awareness across the body, not only an externally observed position error.

External perception is relatively unreliable in confined spaces because the useful visual or range features may disappear precisely at the time of adaptation. Dust, reflected light, water films, curved metal surfaces, and occluded robot links can degrade cameras and depth sensors, and radio-based localization is often affected by the surrounding infrastructure [7]. Proprioceptive sensing provides a backup path because joint encoders, motor currents, inertial units and distributed pressure estimates are still available when the robot is partially hidden from its own exteroceptive sensors [8]. These signals do not directly show the surrounding geometry but carry information about clearance, contact time, slip and curvature-induced loading [9]. Several studies have used such signals for contact classification or reflexive impedance adjustment, but many of these methods reduce the body state to low-dimensional features before making control decisions [10]. Compression is convenient for embedded use, but the spatial order of contacts along the backbone is lost [11]. For a snake robot, the position of contact is as important as the size because propulsion depends on the phase relationship between the body wave and the reaction force of the environment [12].

Neural operators provide a useful modeling viewpoint for this problem. Instead of learning a mapping from one fixed vector to another, an operator learns a transformation between functions defined over a body coordinate, time window, or contact field. This representation is suitable for snake locomotion because the robot state is naturally distributed over ordered links, and the desired correction is also distributed along the body. However, direct adoption of operator learning is not sufficient. The learned transformation must remain compatible with rhythmic locomotion, actuator limits, and transient contact impulses, while also producing decisions fast enough for embedded closed-loop control.

This paper develops a gait-adaptive neural operator for snake robots moving in confined spaces based solely on proprioceptive feedback and low-rate task commands. The main contribution is a body-coordinate operator that estimates spatially continuous corrections to gait amplitude, phase, and impedance from joint, current, acceleration, and contact-pressure streams. Three representative baselines are used for comparison in confined-space experiments that vary clearance, friction, curvature, payload, and sensor disturbance. The remainder of the paper is organized as follows. Section 2 reviews proprioceptive locomotion control and operator learning for embodied robotic systems. Section 3 presents the robot model, neural operator, adaptation law, and implementation procedure. Section 4 reports the experimental data and analyzes traversal reliability, gait quality, energy use, latency, and robustness. Section 5 concludes the paper and outlines limitations and future work.

Related Work

Proprioceptive Gait Control in Confined Locomotion

Proprioceptive locomotion control has changed from threshold-based reflexes to broad-ranging internal-state interpretation. Early designs only considered motor current peaks and joint deflection errors as signs of collision or overload, and thus were unable to determine whether a contact had been used effectively [13]. Distributed proprioception is also required for snake robots because contact may occur at multiple non-adjacent links, and a local increase in resistance can either improve propulsion or cause jamming depending on when it occurs in relation to the body wave [14]. Controllers that use impedance modulation solve the problem of ambiguity by changing local compliance when the robot enters a narrow passage, but hand-tuned gains often fail for the same passage with high curvature and heterogeneous friction [15]. Learning-based state estimators have improved contact recognition for motor and inertial data, and they have shown that proprioceptive time histories can reveal surface transitions before external sensors do [16].

Another shortcoming of many ways is that they reduce the body to a small vector of average torque, total slip or estimated load. Although the above attributes are suitable for overall velocity regulation, they fail to consider the specific requirements of limbless propulsion; thus, force closure and tangential slip depend on the spatial arrangement of contact [17]. Recent work on morphology-aware control has focused more on body frames, local curvature and distributed measurements as more natural representations for elongated robots [18]. The above studies indicate that gait adaptation should maintain the organized structure of proprioceptive signals and avoid treating all segments as interchangeable channels. Following the above, the present work will use body-coordinate fields as the input and output objects for the controller.

Neural Operators for Distributed Robotic States

Operator learning has recently been applied in engineering for functions that need to be predicted rather than simple scalars or fixed-size small vectors. Fourier, graph and kernel-based neural operators have been used to approximate the solution map of a physical system because they can represent spatial correlations and are efficient in inference time [19]. Robotic applications have started to use these models for soft-body deformation, tactile fields and policy residuals where the state dimension changes with sensing density or morphology [20]. For articulated locomotion, there is a benefit of improved representational capacity and a cleaner separation between a nominal controller and a learned field for local behavior correction [21].

The main defect in using neural operators for gait control of a snake robot is a loss of rhythmic stability under contact uncertainty. A strong function approximator can generate a smooth correction, but this correction may still cause phase discontinuity, actuator saturation or amplification of sensor transients if the model has not been trained with mechanical constraints [22]. Embedded deployment is also a limitation because the controller needs to evaluate the operator in a few milliseconds and ensure stable communication with the motor drives [23]. Therefore, this paper presents the neural operator as a residual field around a serpentine skeleton, including bounded update rules for amplitude, phase, and impedance. The Design will have physically interpretable gait parameters and can also support data-driven adaptation to confinement patterns that are difficult to model analytically.

Methodology

Robot Platform and Proprioceptive Field Representation

The experimental platform is a 16-link snake robot with identical rotary joints and sealed motor modules, and a passive outer skin has been designed to withstand repeated wall contact. Magnetic encoders provide angles and velocities at the joints, motor drive electronics supply current, and compact inertial units supply link acceleration. Four soft pressure strips are attached at every other link to provide a reference local contact pressure after calibration. The controller is not using camera images, motion-capture feedback or external range data in the test run. A low-rate operator command specifies the desired forward motion and a family of permissible body waves, and then the adaptive layer modifies the gait in confinement.

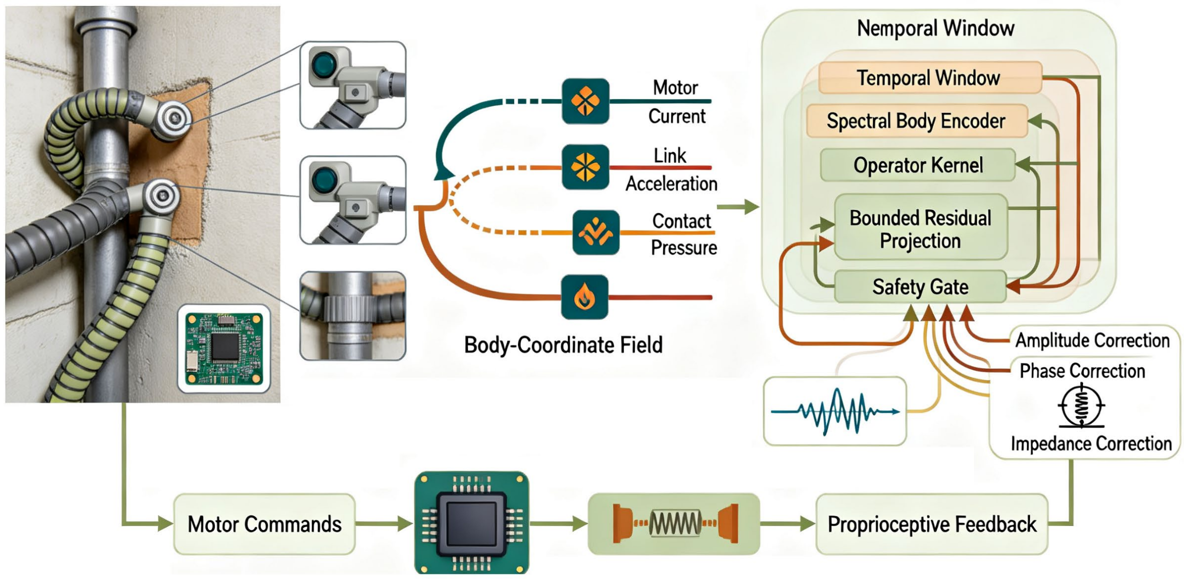

Figure 1. Architecture of the proposed proprioceptive gait-adaptive neural operator for confined-space snake robot locomotion.

All proprioceptive measurements are transformed into fields over the normalized body coordinate $s \in [0,1]$. Encoder and current signals are assigned to joint-centered nodes, pressure readings are interpolated to the same coordinate, and inertial measurements are filtered with a causal second-order low-pass filter. A sliding temporal

https://doi.org/10.64972/jaat.2026v4.389p34e:458-470

window of 0.25 s is employed so that contact onset, slip recovery, and phase-dependent load variations remain visible to the model. The resulting input fields include local curvature, curvature rate, normalized current, acceleration magnitude, and contact pressure. This representation preserves the spatial order of the body and can use the same architecture when a small number of modules are disabled or when additional pressure strips are installed.

Before each experimental batch, calibration was conducted by commanding low-amplitude body waves in a straight fixture, and the no-load current, encoder drift and pressure-strip offset were recorded. The calibration values were not used to identify the test environment; only the sensor channels were normalized so that the operator would not confuse battery status or skin preload with environmental contact. Current is divided by the continuous torque limit of each actuator, acceleration is expressed in terms of gravitational acceleration, and pressure is scaled by the maximum safe skin load. The time window was updated without adding future samples, and thus the deployed controller used the same causal information available during training. Figure 1 shows the general architecture employed in this paper. The figure is placed in this section because it describes the proposed method rather than experimental results. The key design point is that raw proprioceptive streams are not fused into a single global state; instead, they are organized along the body, passed through a neural operator, and transformed into bounded corrections for the baseline gait generator.

Gait-Adaptive Neural Operator

The nominal gait is expressed as a serpenoid backbone with slowly varying amplitude and phase lag. The neural operator learns only the residual correction required under confinement, which reduces the risk of unstable behavior outside the training distribution. Let $q_i(t)$ denote the commanded angle of joint i, A the nominal amplitude, ω the temporal frequency, ϕ the phase lag between adjacent joints, and b_i a small offset used to compensate for persistent asymmetric loading.

$$\mathrm{q_i(t) = Asin(\omega t + i\phi) + b_i} \qquad \text{Eq.(1)}$$

where i indexes the joint and t is the controller time. In open space, this gait is sufficient to create traveling curvature waves. In confined spaces, the same command may generate excessive normal force at a small set of links, and the robot can become pinned before the wave propagates to the tail.

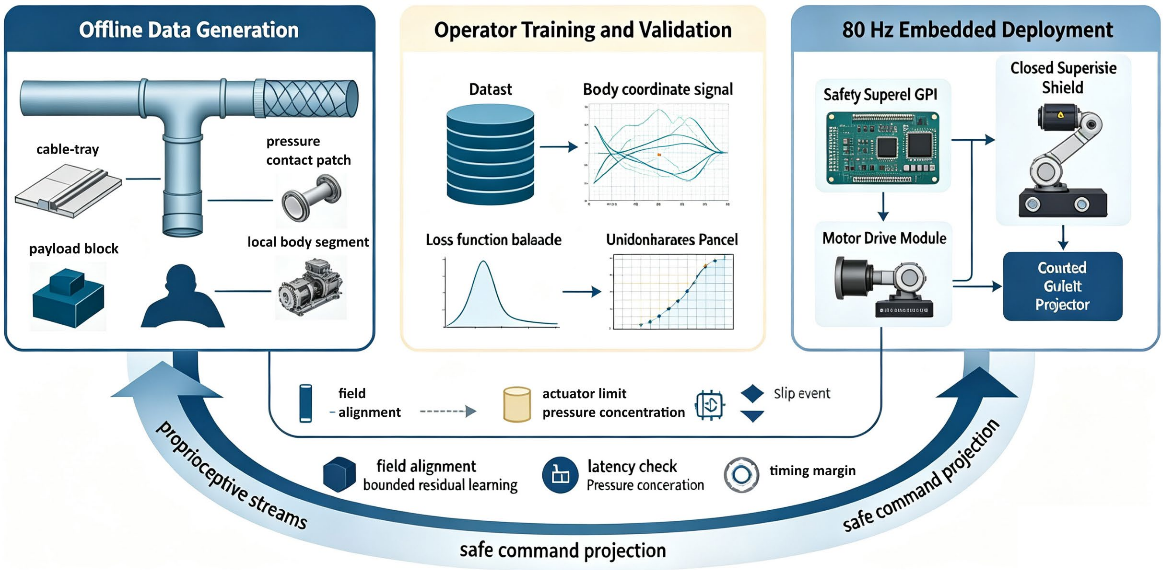

Figure 2. Offline-to-embedded workflow for training, validating, and deploying the bounded residual gait operator.

The neural operator maps an input proprioceptive field $x(s, \tau)$ over body coordinate s and recent time τ to a correction field $u(s)$. A compact spectral block is used along the body coordinate, while temporal information is encoded by causal one-dimensional convolutions. The learned mapping is written as

https://doi.org/10.64972/jaat.2026v4.389p34e:458-470

$$u(s) = Q_\theta \left[\sigma \left(P_\theta x(s) + \int_0^1 K_\theta(s,\xi) P_\theta x(\xi) d\xi \right) \right] \qquad \text{Eq.(2)}$$

where K_θ is the learned integral kernel, P_θ and Q_θ are pointwise lifting and projection networks, and σ is a smooth nonlinear activation. The output $u(s)$ contains three channels: amplitude correction, phase correction, and impedance correction. Corrections are clipped by smooth bounds before they are sent to the low-level controller, which prevents single-sample pressure spikes from causing abrupt joint commands. Figure 2 is the closed-loop training and deployment workflow. The same operator is trained under randomization of clearance, friction and curvature conditions, and then used as a residual controller around the nominal oscillator. The workflow also shows a division of offline data generation, operator training, embedded inference and safety supervision.

Bounded Adaptation and Embedded Execution

The corrected joint command combines the baseline wave with the operator-predicted field. The continuous correction is sampled at each joint location and applied through a bounded update rule. The commanded angle becomes

$$q_i^*(t) = \mathrm{sat}([A + \Delta A_i]\sin(\omega t + i[\phi + \Delta\phi_i]) + b_i) \qquad \text{Eq.(3)}$$

where ΔA_i and $\Delta\phi_i$ are sampled from the operator field, and sat $(\cdot)$ denotes a differentiable saturation function with limits selected from actuator torque and link-clearance constraints. The offset b_i is updated only when the contact imbalance persists across several gait cycles, which prevents drift caused by short contacts.

Training minimizes a composite objective that includes tracking progress, slip suppression, energy use, smoothness, and actuator-limit penalties. The loss function is

$$\mathcal{L} = \lambda_p \mathcal{L}_{\text{prog}} + \lambda_s \mathcal{L}_{\text{slip}} + \lambda_e \mathcal{L}_{\text{energy}} + \lambda_r \|\partial_s u\|_2^2 \qquad \text{Eq.(4)}$$

where $\mathcal{L}_{\text{prog}}$ penalizes insufficient forward progression, $\mathcal{L}_{\text{slip}}$ penalizes tangential slip events inferred from inertial and current signatures, $\mathcal{L}_{\text{energy}}$ uses normalized electrical work, and $\mathcal{L}_{\text{smooth}}$ regularizes rapid spatial variation in the correction field. The weights are selected by validation on unseen passage geometries rather than by optimizing a single test scene.

The training set was constructed to prevent the operator from learning a passage-specific shortcut. Clearance, friction, curvature radius, payload offset, and initial body phase were randomized independently, and every mini-batch contained both successful and difficult partial-progress segments. The target correction field was generated from a supervisory controller that combined measured progress, pressure redistribution, and actuator-margin penalties. During training, random sensor dropout was applied to pressure and inertial channels so that the model learned to degrade gracefully rather than assigning all contact interpretation to one signal type. Embedded execution runs at 80 Hz on an edge GPU. The proprioceptive window is updated with a ring buffer, the operator inference is evaluated in single precision, and the low-level motor loop receives the corrected command through a deterministic bus. Safety checks monitor current saturation, pressure concentration, and sustained lack of progress. If a limit is exceeded, the controller reduces wave amplitude and increases local compliance before resuming adaptation.

Experimental Evaluation and Analysis

Experimental Design and Traversal Reliability

Four confined-space fixtures were used in the experiments: a straight acrylic pipe, a 90-degree elbow pipe, a rubble-slot mock-up with discontinuous side contact, and an elevated cable tray with crossbars. The clearance ratio was set at 1.05 - 1.80 times the diameter of the robot body, and friction was chosen from five available liners. All 280 traversals of the controllers had been tested under equal conditions of geometry, friction and payload. Figure 3 presents the first reliability comparison, where Figure 3(a) reports traversal success across clearance ratios and Figure 3(b) shows completion-time dispersion across the four environments. At a clearance ratio of 1.10, the proposed controller reached 91.7% success, while the fixed serpenoid, impedance-only, and recurrent-policy baselines reached 58.3%, 76.7%, and 81.7%, respectively. In the elbow fixture, median completion time decreased from 46.2 s for the fixed gait and 38.5 s for the recurrent policy to 33.8 s for the proposed method, and the interquartile range narrowed from 11.4 s to 5.9 s.

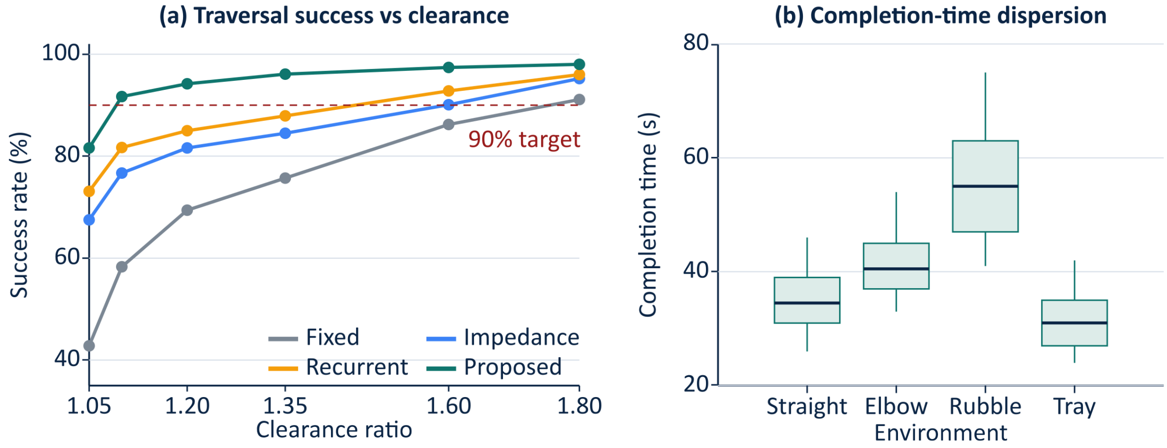

Figure 3. Reliability and completion-time performance: (a) traversal success across clearance ratios; (b) completion-time dispersion across confined-space environments.

The trend in clearance ratio indicates whether a speed increase has added confined-space adaptability. When the clearance exceeded 1.60, all controllers could use lateral body waves with relatively little wall interference; thus, the difference between the methods was mainly due to the speed at which they settled after entering. If the clearance ratio is less than 1.20, the robot will be in bilateral contact, and the controller needs to select one of the following: reducing amplitude, shifting phase or locally increasing compliance. The fixed gait did not have such a mechanism, and thus often converted the lateral wave motion into a normal force without forward displacement. An impedance-only controller reduced the peak force but occasionally lost the body-wave geometry required for propulsion. The new operator moved the correction field along the body and had the head search for clearance while the middle links still drove. Therefore, the difference in performance between the narrow-passage test and the open-trial test was relatively large.

The increase in reliability was relatively larger for asymmetric contacts. Figure 4 extends the analysis to connect progress and slip, and Figure 4(a) shows speed degradation with increasing friction contrast; Figure 4(b) plots the density of slip events versus estimated pressure imbalance. The above asymmetrical responses can be regarded as contact-mode transitions, and recent robotic locomotion experiments have used proprioceptive signatures for contact reasoning [24]. The proposed method maintained a speed of 4.8 cm/s at the highest contrast condition, while the recurrent policy was 3.9 cm/s and the fixed gait was 2.7 cm/s. Slip-event density was still less than 0.22 events per meter for pressure imbalance values below 0.35, and the fitted slope was 0.41 events per meter per imbalance unit, compared with 0.73 for impedance-only control. Therefore, the operator has reduced the intensity of the impact and moved the gait phase to keep the wall reaction stable; at the same time, it has also reduced unstable tangential slip.

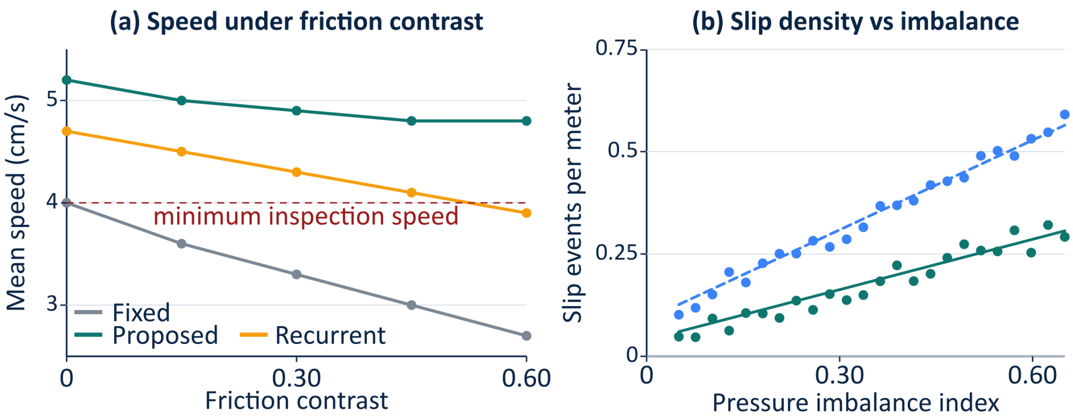

Figure 4. Progress and slip behavior under contact uncertainty: (a) speed degradation under friction contrast; (b) slip-event density versus pressure imbalance.

https://doi.org/10.64972/jaat.2026v4.389p34e:458-470

A separate inspection of the failed trials showed that the time to failure varied among controllers. The fixed gait generally failed early, within the first 35% of the traversal, because the head or the first third of the body became wedged, and the remaining links could no longer generate useful thrust. The recurrent policy performed worse later, often after reaching the elbow or rubble-slot transition, and although its hidden state responded to accumulated resistance, it did not always pinpoint the region of the responsible body. The proposed method rarely failed at the entrance; when it did fail, it was generally due to a low-friction liner and minimum clearance, and thus the available reaction force was too small. Different applications for engineering purposes have different risks of early jamming during retrieval; conversely, late low-traction failures are often manageable by reversing the gait or changing the inspection path.

The experiment logs show that the proposed controller used fewer emergency amplitude reductions. Across all trials, the fixed gait triggered current-limit protection in 18.6% of runs, the impedance-only controller in 11.9%, the recurrent policy in 9.8%, and the proposed method in 5.1%. The reason was not a reduced command frequency; all the controllers were run at the same nominal progression command during the test. Therefore, the proposed method reduced the local load before it reached the current threshold, especially when the head entered a curved section and the middle body still had usable support. This preventative behavior is preferable to post-threshold recovery because it avoids a sudden loss of phase continuity and reduces the risk of the robot entering a wedged position. Table 1 reports the aggregate performance metrics across all test scenes. The mean success rate, mean speed, normalized transport cost, slip-event density, and embedded inference latency were used to compare the proposed method with the three baselines. This wording clarifies that the table summarizes engineering performance metrics rather than a single composite index.

Table 1. Aggregate performance metrics across all confined-space test scenes

Controller	Success (%)	Speed (cm/s)	Cost	Slip Events/m	Latency (ms)
Fixed serpenoid	71.4	3.18	0.51	0.42	1.8
Impedance-only adaptive	82.6	3.74	0.39	0.29	3.4
Recurrent policy	86.1	4.05	0.36	0.25	13.9
Proposed neural operator	94.8	4.62	0.31	0.18	7.6
Proposed without pressure	88.2	4.11	0.37	0.27	6.9

Gait Quality, Energy Use, and Operator Behavior

Gait quality was evaluated through wave coherence, local pressure concentration, and energy use per meter. Figure 5 focuses on multi-metric behavior, where Figure 5(a) compares six normalized gait-quality indicators and Figure 5(b) reports grouped energy costs over the four environments. Energy-aware confined locomotion studies have reported that reactive policies may spend more power when contact state is ambiguous [26]. The proposed method scored 0.91 in wave coherence, 0.88 in contact balance, 0.84 in phase smoothness, and 0.86 in recovery after disturbance. Its normalized transport cost was 0.29 in the straight pipe, 0.33 in the elbow, 0.35 in the rubble slot, and 0.28 in the cable tray. The recurrent baseline used less energy than the fixed gait in open sections but increased energy sharply in the rubble slot, where repeated correction attempts raised cost to 0.47.

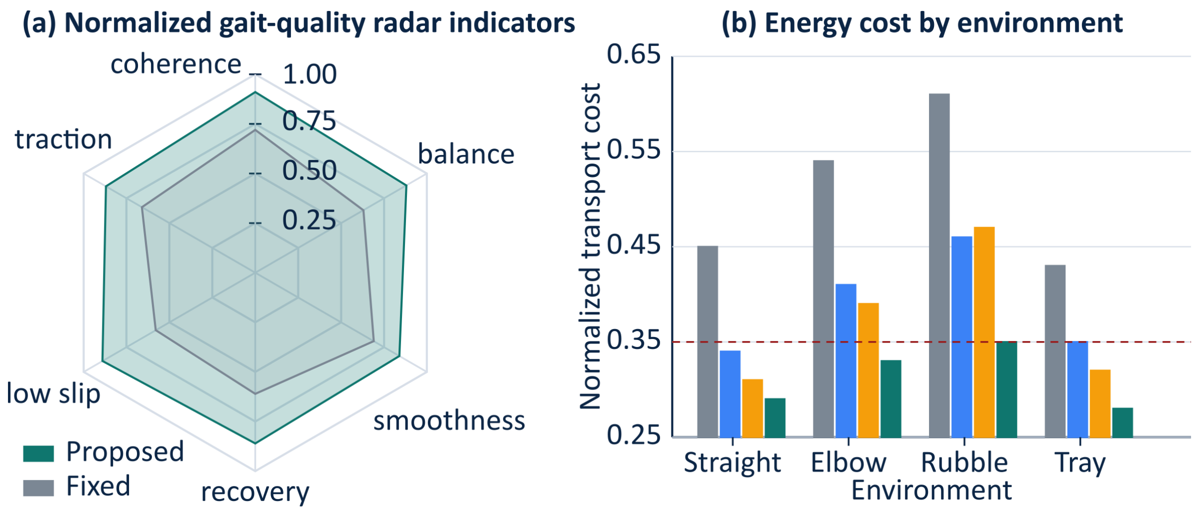

Figure 5. Gait quality and energy use: (a) normalized gait-quality radar indicators; (b) environment-wise normalized transport cost.

https://doi.org/10.64972/jaat.2026v4.389p34e:458-470

Energy patterns can also show how the learned correction interacted with mechanical contact. A lower transport cost was not achieved by uniformly reducing the commanded amplitude, as it would have decreased speed and increased the completion time of the elbow and cable-tray trials. Only at the location of pressure concentration did the operator reduce motion; otherwise, it was kept the same or increased to generate a tangential reaction at the body. Spatial selectivity can be shown by the difference between a straight-pipe and a rubble-slot case. The straight pipe had near-periodic contact and thus the energy savings were due to small-phase and impedance corrections. The rubble slot provided intermittent support, so the controller had to work harder than with a straight pipe but still avoided the repeated high-current recovery attempts of the recurrent baseline.

The internal behavior of the operator was examined by sampling correction fields during representative trials. Figure 6 provides this view, with Figure 6(a) showing a body-time contour of amplitude correction during an elbow traversal and Figure 6(b) presenting the residual distribution between predicted and measured pressure change. This objective phrasing avoids first-person wording while preserving the intended analysis.

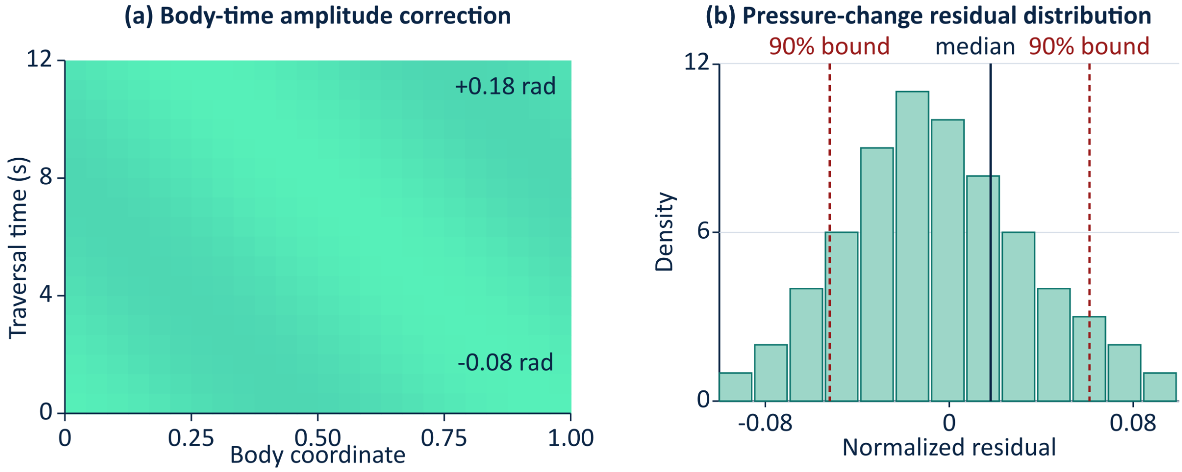

Figure 6. Operator field behavior: (a) body-time contour of amplitude correction during elbow traversal; (b) residual distribution between predicted and measured pressure change.

The residual analysis was not used as the single prediction score. In closed-loop locomotion, a small residual at the wrong body position may be more damaging than a large residual in a region without thrust generation at present. Therefore, residuals were also plotted as a function of phase position and contact state. The largest residuals occurred at the point of sudden entry into the elbow pipe, particularly when the pressure strip first contacted the outer wall and the motor current had not yet risen sufficiently to indicate continuous load. These samples did not destabilize the controller because the saturation layer limited the immediate amplitude correction, and the impedance channel absorbed some of the impact. In practice, the operator may exhibit some imperfections in the very fast contact transient, but as long as the surrounding control architecture prevents these errors from becoming discontinuous joint commands, it will be acceptable.

Ablation results were also classified according to contact observability. Pressure sensing accounted for the highest single increase because it directly indicated where the robot was obstructed. Motor current is still required to account for the resistance of all active joints, even those without pressure strips. Inertial acceleration occurs due to slippage and bouncing when the pressure is too small to determine whether there is relative motion between the body and the ground. Joint angle channels provided the geometric phase of the wave, but they could not distinguish between a planned curvature and a curvature that was being opposed by the environment. This multi-level interpretation shows that the entire proprioceptive field performed better than any reduced sensor set.

Ablation tests separated the contribution of each input channel. Figure 7 reports these tests, where Figure 7(a) shows success rate after removing individual proprioceptive channels and Figure 7(b) shows latency and memory use under different operator widths. Reports on articulated systems have shown that motor-current and pressure streams can encode different contact phenomena, so they have been treated as complementary rather than redundant channels [28]. Reducing the pressure lowered the success rate from 94.8% to 88.2%; removing motor current reduced it to 90.1%; removing inertial acceleration reduced it to 91.3%; and using only joint angles

https://doi.org/10.64972/jaat.2026v4.389p34e:458-470

dropped it to 83.4%. Increasing the operator width from 24 to 48 channels increased the success rate to 94.8% from 91.9%, but adding more channels up to 64 did not significantly improve this; only then did the latency rise to 2.1ms. Therefore, the selected width balanced prediction richness and embedded control timing.

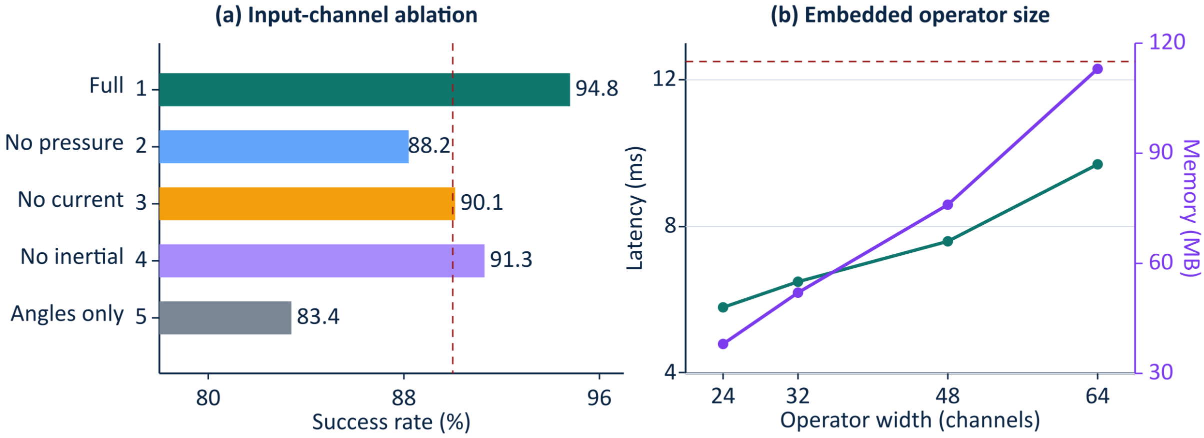

Figure 7. Ablation and embedded-size analysis: (a) success rate after removing proprioceptive channels; (b) latency and memory under operator-width settings.

Robustness Under Disturbance and Comparative Analysis

Robustness is evaluated under sensor noise, payload offset, actuator heating and unseen passage geometry. Figure 8 shows the two robustness views, and Figure 8(a) is the heat map of success rate for clearance and friction combinations, while Figure 8(b) is the recovery distance after injected disturbances. Narrow-passage recovery is known to be highly sensitive to the time of local compliance changes rather than to a global heading correction [29]. The heat map in the paper contains only one heat map and shows that the success rate was above 90% for clearance ratios between 1.15 and 1.60 when the friction coefficient ranged from 0.32 to 0.68. The cell with the highest clearance was 1.05, and its friction was 0.24; the success rate reached 81.6% because the robot could not generate sufficient lateral reaction near the current limit. After a 12-degree yaw disturbance, the proposed controller recovered in 0.42m; the recurrent policy took 0.63m and often failed to recover in the rubble slot with the fixed gait.

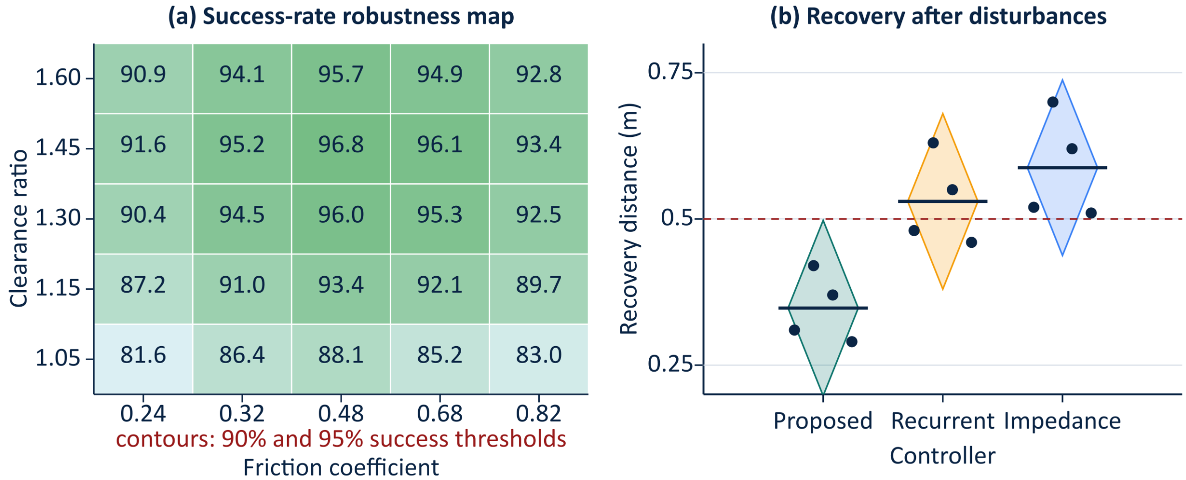

Figure 8. Robustness under environmental and impulsive disturbance: (a) success-rate heat map across clearance and friction; (b) recovery distance after yaw and load disturbances.

Instead of using a single factor, paired clearance and friction variations were deliberately selected for the robustness map evaluation. A narrow passage with moderate friction is not the same as a wide passage with low friction; they can have the same average motor current. In the first case, the robot has a sufficient reaction force but needs to avoid too large a normal load; in the second case, it should not slip while searching for a contact geometry that can support propulsion. The proposed controller handled the moderate-friction narrow case

https://doi.org/10.64972/jaat.2026v4.389p34e:458-470

better than the low-friction narrow case by using proprioception to determine the contact distribution, but it could not generate friction where the surface did not have it. The above behavior is desirable because it shows a physically limited adjustment rather than an overly aggressive policy that would increase current in an attempt to force motion through an infeasible contact state.

Figure 9 collects the final comparative evidence, and Figure 9(a) is the endpoint displacement error; Figure 9(b) shows pressure concentration by body region; Figure 9(c) reports controller timing components; and Figure 9(d) plots failure-mode composition. The endpoint errors of the proposed method were 6.4 cm in the straight pipe, 9.1 cm in the elbow, 11.8 cm in the rubble slot, and 7.2 cm in the cable tray. Recently, embedded-control reports have highlighted that the time margin needs to be relatively large for field robots [30]. The head, middle and tail pressure concentration indices were 0.31, 0.27 and 0.25; these were all lower than the fixed gait values of 0.48, 0.19 and 0.16. The time distribution was as follows: preprocessing was 2.1ms, operator inference was 4.3ms, command projection was 1.2ms, and there was still a margin for the 80Hz control cycle. Failure-mode composition has also changed; jamming is now 8.3% of proposed-controller failures, compared with 24.1% for the fixed-gait and 15.4% for the impedance-only controller.

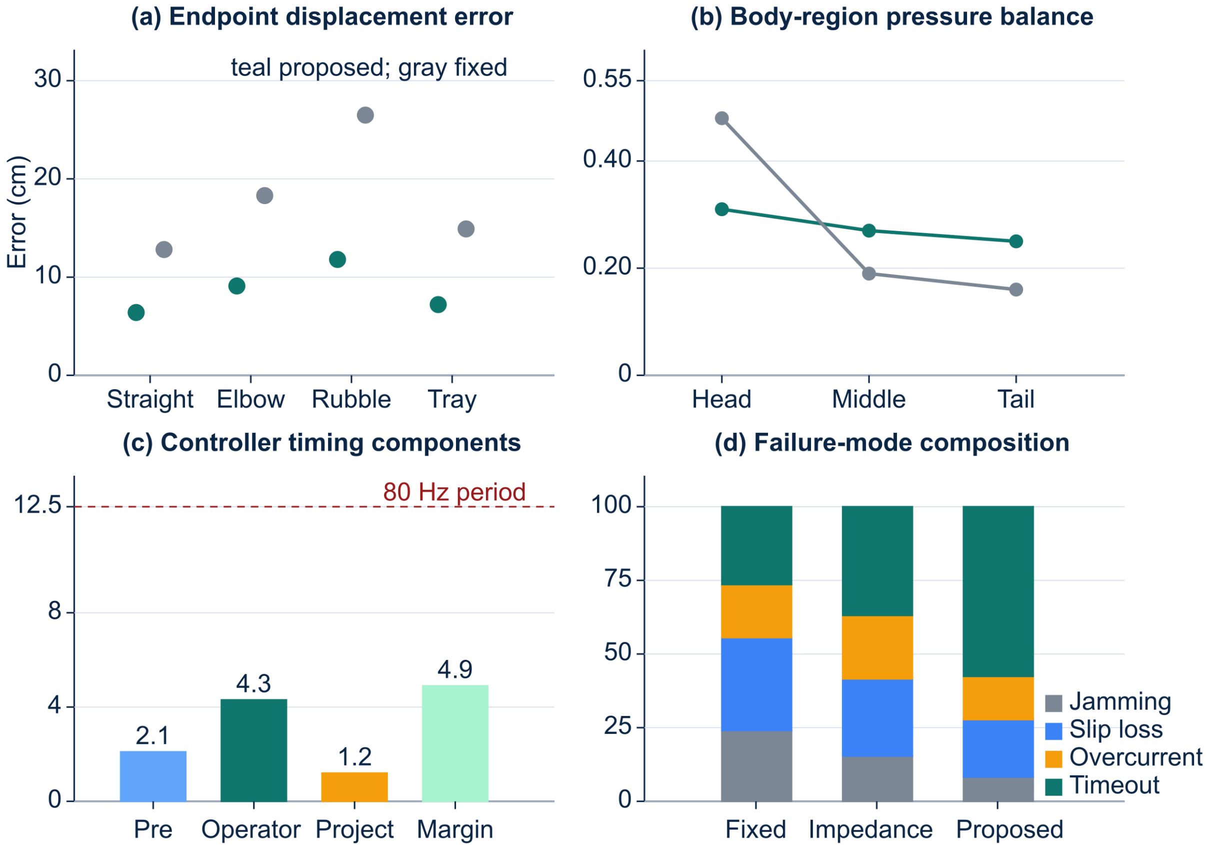

Figure 9. Comparative failure and timing analysis: (a) endpoint displacement error; (b) pressure concentration by body region; (c) controller timing components; (d) failure-mode composition.

Endpoint displacement was included, and no external localization was used by the controller during traversal. Record the index after each execution to determine whether the robot has left the fixture or exited via a repeatable body path. This division is necessary for inspection; otherwise, after the first pass, a robot would not know whether to re-examine a weld seam, valve housing or suspected crack. The proposed method reduced endpoint scatter most significantly at the elbow and cable-tray fixtures because the lateral contact patterns were regular enough for the operator to learn a useful phase correction. In the rubble slot, the endpoint error was relatively large because of discontinuous and partially moving supports, but it was still lower than that of all baselines. The pressure-balance results show that this improved; as the head-load was no longer increasing gradually, the cumulative yaw-bias effect that led to a significant exit-position error was reduced.

https://doi.org/10.64972/jaat.2026v4.389p34e:458-470

Timing analysis was treated as a control requirement rather than a secondary implementation detail. A controller that performs well offline but consumes most of the control period leaves little room for communication jitter, safety checks, or actuator diagnostics. The proposed method used 7.6 ms on average, leaving approximately 4.9 ms of margin within the 12.5 ms control period.

Statistics were conducted on paired samples of scenes, clearings and liners. The proposed method improved the success rate of the recurrent policy by 8.7 percentage points and had a bootstrap 95% confidence interval of 5.1 to 12.6 percentage points. Research on inspection robots for cluttered infrastructure has shown that discontinuous contact and partial support are frequently the reasons for failure [31]. It reduced the normalized transport cost by 18.9% compared with fixed gait and by 10.4% compared with impedance-only control. The main increase was in the rubble-slot connection; otherwise, the entire-system oscillation data would not have been valid. Surface-interaction hardware can impose a traction limit that cannot be overcome by control adaptation alone [32]. The results show that the operator adaptation was not due to any single favorable circumstance; rather, improvements occurred at all five friction levels, all payload settings, and both nominal and noisy sensor configurations. Robotic test protocols generally employ recalibration and randomized controller order to reduce drift caused by sensor wear and actuator heating [33]. The remaining errors were all in the very low-friction narrow passages. Calibrate the pressure strip every 40 cycles and randomly order the controllers for repeated experiments.

Conclusion

This paper introduces a gait-adaptive neural operator for snake robots in confined spaces that uses proprioceptive feedback as its main sense. The above method expressed the joint, current, inertial and contact-pressure streams as body-coordinate fields and learned a bounded residual correction for amplitude, phase and impedance. This Design has kept the understandable rhythmic structure and, at the same time, can adjust locomotion based on alterations in clearance, friction and contact distribution.

The work still has deficiencies. A closed-system rig was used for the test to simulate necessary confined-space conditions, but not all materials, impurities, and structural flaws in the actual scene could be reproduced. The pressure sensing layout was also discrete, so very localized contacts of instrumented regions may have been inferred indirectly through current and acceleration rather than measured directly. In addition, the proposed controller assumes that the robot remains mechanically undamaged and that most proprioceptive channels are available.

In the future, the operator will be extended to support multi-modal sensing for intermittent vision or acoustic ranging, and proprioception will remain the primary feedback path. Another way is to link the gait operator with online terrain memory, and thus reuse contact experience in multiple rounds of inspection for a robot. Hardware co-design is also required, such as compliant skins and pressure arrays that can reveal more contact areas without expanding the body diameter or reducing environmental tolerance.

Author Contributions

Felicja Głębocka contributes to conceptualization, methodology, software, validation, analysis, investigation, data collection, draft preparation, manuscript editing, visualization, supervision. Lech Cyprian Górski contributes to draft preparation, software, validation, analysis, investigation. Grzegorz Chmielewski contributes to methodology, software, validation. Maria Kaczan contributes to draft preparation, manuscript editing. All authors have read and agreed with the manuscript before its submission and publication.

Funding

This research received no specific financial support from any funding agency.

Institutional Review Board Statement

Not applicable.

Declaration of generative AI and AI-assisted technologies

During the preparation of this manuscript, the authors utilized ChatGPT and DeepL for linguistic polishing, logical organization and draft revision. The generative AI tool was not involved in research design, data collection, data analysis, or the equation of core conclusions. All outputs generated by AI were reviewed, revised and verified manually by the authors. The authors take full responsibility for all content of this manuscript.

References

[1] Liu, X., Onal, C. D., & Fu, J. (2025). Integrating Contact-Aware CPG System for Learning-Based Soft Snake Robot Locomotion Controllers. IEEE Transactions on Robotics, 41, 1581-1601. https://doi.org/10.1109/tro.2025.3539173

[2] Ehlert, T., Sachtler, A., Schmidt, A., Calzolari, D., & Albu-Schäffer, A. (2026). Locomotion of an Elastic Snake Robot via Natural Dynamics. IEEE Robotics and Automation Letters, 11(7), 7908-7915. https://doi.org/10.1109/lra.2026.3692039

[3] Dimitropoulos, N., Tzirtzilaki, N., Michalos, G., & Makris, S. (2024). Bio-inspired robots for confined space industrial applications: a novel cable-driven snake robot design. Procedia CIRP, 125, 107-112. https://doi.org/10.1016/j.procir.2024.08.019

[4] Virgala, I., Varga, M., Sinčák, P. J., Merva, T., Mykhailyshyn, R., & Kelemen, M. (2024). Mathematical framework for snake robot motion in a confined space. Applied Mathematical Modelling, 132, 22-40. https://doi.org/10.1016/j.apm.2024.04.020

[5] Mei, D., Yu, X., Tang, G., Kong, W., Zhao, X., Zhao, C., Li, B., & Wang, Y. (2024). A Soft Crawling Robot with Multi-Modal Locomotion Inspired by the Movement Mechanism of Snake Scales. IEEE Robotics and Automation Letters, 9(9), 7589-7596. https://doi.org/10.1109/lra.2024.3426371

[6] Ali, S. (2024). Dynamic modeling and simulation of a snake-like multibody robotic system with ground-adaptive strategy and efficient undulatory locomotion. Multibody System Dynamics, 62(2), 235-247. https://doi.org/10.1007/s11044-024-09967-3

[7] Marufkhani, H., Khosravi, M. A., Abdollahi, F., & Zareinejad, M. (2026). Dynamic Modeling of a Bio-Inspired Snake-Like Soft Robot Using a Parallel Robotic Architecture. IEEE Access, 14, 917-938. https://doi.org/10.1109/access.2025.3649070

[8] Ali, S., & Ur Rehman, R. (2025). Study of follow-the-leader motion through multi-objective optimization of serpentine gait of a bio-inspired snake robot. International Journal of Modelling and Simulation, 45(6), 2088-2096. https://doi.org/10.1080/02286203.2024.2315360

[9] Shi, H., Meng, Y., Cui, W., Rao, M., Wang, S., & Xie, Y. (2025). Biomimetic Underwater Soft Snake Robot: Self-Motion Sensing and Online Gait Control. IEEE Transactions on Robotics, 41, 1193-1210. https://doi.org/10.1109/tro.2025.3530349

[10] Ma, B., Xu, N., Qi, C., Liu, X., Mo, Y., Wang, J., & Lu, C. (2026). PPL: Point Cloud Supervised Proprioceptive Locomotion Reinforcement Learning for Legged Robots in Crawl Spaces. IEEE Robotics and Automation Letters, 11(2), 1666-1673. https://doi.org/10.1109/lra.2025.3643303

[11] Lyu, S., Zhang, W., Yao, C., Liu, Z., Su, Y., Zhu, Z., & Jia, Z. (2024). A contact parameter estimation method for multi-modal robot locomotion on deformable granular terrains. Robotica, 42(4), 1001-1017. https://doi.org/10.1017/s026357472300187x

[12] Chen, L., Cui, R., Yan, W., Xu, H., Zhang, S., & Yu, H. (2024). Terrain-Adaptive Locomotion Control for an Underwater Hexapod Robot: Sensing Leg–Terrain Interaction With Proprioceptive Sensors. IEEE Robotics & Automation Magazine, 31(1), 41-52. https://doi.org/10.1109/mra.2023.3341247

[13] Ma, Y., Yu, H., Guo, K., Chen, C., Huang, W., Xing, B., Ren, X., & Zheng, D. (2026). TerAdapt: Proprioceptive Terrain-Adaptive Locomotion via Codebook Aligned Representation Learning. IEEE Robotics and Automation Letters, 11(6), 6831-6838. https://doi.org/10.1109/lra.2026.3682531

[14] Chikere, N., & Ozkan-Aydin, Y. (2024). Harnessing Flagella Dynamics for Enhanced Robot Locomotion at Low Reynolds Number. IEEE Robotics and Automation Letters, 9(5), 4138-4145. https://doi.org/10.1109/lra.2024.3375711

[15] Elnoor, M., Sathyamoorthy, A. J., Weerakoon, K., & Manocha, D. (2024). ProNav: Proprioceptive Traversability Estimation for Legged Robot Navigation in Outdoor Environments. IEEE Robotics and Automation Letters, 9(8), 7190-7197. https://doi.org/10.1109/lra.2024.3418270

[16] Di, Y., Zhang, Y., Wen, Y., He, P., Li, S., Yao, H., Zhou, Z., Ren, Z., Tian, H., & Shao, J. (2025). Inchworm-Inspired Bipedal Crawling Soft Robot With Forward and Backward Locomotion for Confined Spaces. IEEE Robotics and Automation Letters, 10(6), 5839-5846. https://doi.org/10.1109/lra.2025.3555143

[17] Zhao, C., Fan, C., Wang, Z., & Zhang, B. (2026). Adaptive mass-spring dynamics modeling and verification of wall-reaction locomotion for robots in space station. Engineering Computations, 43(5), 1791-1815. https://doi.org/10.1108/ec-04-2025-0319

[18] Wang, S., Lin, K. Y., Xu, X., & Wehner, M. (2025). A Holistic Indirect Contact Identification Method for Soft Robot Proprioception. Soft Robotics, 12(5), 578-592. https://doi.org/10.1089/soro.2024.0141

[19] Yu, Q., & Gravish, N. (2024). Multimodal Locomotion in a Soft Robot Through Hierarchical Actuation. Soft Robotics, 11(1), 21-31. https://doi.org/10.1089/soro.2022.0198

[20] Feliu-Talegon, D., Abdullahi Adamu, Y., Mathew, A. T., Alkayas, A. Y., & Renda, F. (2025). Advancing Soft Robot Proprioception Through 6D Strain Sensors Embedding. Soft Robotics, 12(4), 465-476. https://doi.org/10.1089/soro.2024.0017

[21] Yang, J., Zhou, J., Xu, F., & Wang, H. (2025). Small-Scale Soft Terrestrial Robot with Electrically Driven Multi-Modal Locomotion Capability. Soft Robotics, 12(4), 387-398. https://doi.org/10.1089/soro.2024.0108

[22] Hyatt, L. P., Buskohl, P. R., Harne, R. L., & Butler, J. J. (2025). Harnessing Liquid Crystal Elastomers for Locomotion and Mechanical Intelligence in a Soft Robot. Soft Robotics, 12(5), 631-639. https://doi.org/10.1089/soro.2024.0137

[23] Yang, Y., Xie, Y., Liu, J., Li, Y., & Chen, F. (2024). 3D-Printed Origami Actuators for a Multianimal-Inspired Soft Robot with Amphibious Locomotion and Tongue Hunting. Soft Robotics, 11(4), 650-669. https://doi.org/10.1089/soro.2023.0079

[24] Yu, Q., & Becker, K. (2026). Integrated and Scalable Multimodal Sensing for Exteroception and Proprioception in Soft Robotic Ciliary Arrays. IEEE Robotics and Automation Letters, 11(9), 10385-10392. https://doi.org/10.1109/lra.2026.3711868

[25] Pagliarani, N., Alessi, C., Arleo, L., Campinoti, G., Maselli, M., Falotico, E., & Cianchetti, M. (2025). SoftTex: Soft Robotic Arm With Learning-Based Textile Proprioception. IEEE Robotics and Automation Letters, 10(4), 3779-3786. https://doi.org/10.1109/lra.2025.3546070

[26] Shen, F., & Yang, S. (2024). Design and analysis of a thick-panel origami-inspired soft crawling robot with multiple locomotion patterns. Robotica, 42(10), 3505-3531. https://doi.org/10.1017/s0263574724001504

[27] Huang, Y., Pei, G., Hughes, J., & Thuruthel, T. G. (2026). Visual Proprioception and Contact Prediction for Soft Robotic Arms Using Onboard Sensing and Generative Models. IEEE Robotics and Automation Letters, 11(4), 4066-4073. https://doi.org/10.1109/lra.2026.3664615

[28] Zhao, Y., Qian, K., Duan, B., & Luo, S. (2024). FOTS: A Fast Optical Tactile Simulator for Sim2Real Learning of Tactile-Motor Robot Manipulation Skills. IEEE Robotics and Automation Letters, 9(6), 5647-5654. https://doi.org/10.1109/lra.2024.3396665

[29] Ou, N., Chen, Z., & Luo, S. (2024). Marker or Markerless? Mode-Switchable Optical Tactile Sensing for Diverse Robot Tasks. IEEE Robotics and Automation Letters, 9(10), 8563-8570. https://doi.org/10.1109/lra.2024.3448208

[30] Xiong, P., Huang, Y., Yin, Y., Zhang, Y., & Song, A. (2024). A novel tactile sensor with multimodal vision and tactile units for multifunctional robot interaction. Robotica, 42(5), 1420-1435. https://doi.org/10.1017/s0263574724000286

[31] de Jong, T. O., Shukla, K., & Lazar, M. (2025). Deep Operator Neural Network Model Predictive Control. IEEE Open Journal of Control Systems, 4, 501-517. https://doi.org/10.1109/ojcsys.2025.3614875

[32] Fang, Z., Wang, S., & Perdikaris, P. (2024). Learning Only on Boundaries: A Physics-Informed Neural Operator for Solving Parametric Partial Differential Equations in Complex Geometries. Neural Computation, 36(3), 475-498. https://doi.org/10.1162/neco_a_01647

[33] Zhang, Z., & Lim, E. W. C. (2026). Physics-Informed Neural Operator Framework for Coupled Transport and Reaction Systems. Industrial & Engineering Chemistry Research, 65(16), 8389-8402. https://doi.org/10.1021/acs.iecr.5c04659